

Curvature Radiation in Rotating Pulsar Magnetosphere

P. F. Wang^{*}, C. Wang, and J. L. Han

National Astronomical Observatories, Chinese Academy of Sciences. A20 Datun Road, Chaoyang District, Beijing 100012, China

27 November 2024

ABSTRACT

We consider the curvature emission properties from relativistic particles streaming along magnetic field lines and co-rotating with pulsar magnetosphere. The co-rotation affects the trajectories of the particles and hence the emission properties, especially the polarization. We consider the modification of the particle velocity and acceleration due to the co-rotation. Curvature radiation from a single particle is calculated using the approximation of a circular path to the particle trajectory. Curvature radiation from particles at a given height actually contains the contributions from particles streaming along all the nearby field lines around the tangential point, forming the emission cone of $1/\gamma$. The polarization patterns from the emission cone are distorted by the additional rotation, more serious for emission from a larger height. Net circular polarization can be generated by the density gradient in the emission cone. For three typical density models in the form of core, cone and patches, we calculate the polarization profiles for emission generated at a given height. We find that the circular polarization could have a single sign or sign reversal, depending on the density gradient along the rotation phase. The polarization profiles of the total curvature radiation from the whole open field line region, calculated by adding the emission from all possible heights, are similar to that from a dominating emission height. The circular polarization of curvature radiation has sign reversals in the patchy emission, while it has a single sign for the core emission, and is negligible for the cone emission.

Key words: curvature radiation - rotation - relativistic particles - pulsars: general

1 INTRODUCTION

Pulsar radio emission is generally believed to be generated by relativistic particles streaming out along the open magnetic field lines in pulsar magnetosphere. The observed radio emission are generally highly linearly polarized, and have significant circular polarization (Lyne & Manchester 1988; Han et al. 1998; Rankin & Ramachandran 2003). Various radio emission mechanisms are suggested to explain polarization profiles (e.g. Beskin et al. 1988; Xu et al. 2000; Gangadhara 2010).

Curvature radiation serves as one of the most possible emission mechanisms for pulsar radio emission. Buschauer & Benford (1976) firstly developed the general formalism for coherent curvature radiation by a relativistic plasma streaming along curved trajectories using antenna mechanism, assuming the plasma is perturbed by a plane wave. Benford & Buschauer (1977) applied this mechanism for pulsar radio emission and calculated the luminosity. Ochelkov & Usov (1980) analytically calculated the pulsar emission spectrum from curvature radiation. In polarization

aspect, it is known that curvature radiation is almost completely linearly polarized. Gil & Snakowski (1990) pointed out the sign reversal feature for circular polarization (CP) of core emission. Gangadhara (2010) considered the geometry of the emission region in pulsar magnetosphere, obtained the polarization states self-consistently, and explained the correlation between the position angle (PA) and the sign reversal of CP (Han et al. 1998).

Because pulsar magnetosphere is co-rotating with the neutron star, the streaming particles should have co-rotation velocity additional to the streaming velocity along the magnetic field line, which affects the curvature radiation properties. Blaskiewicz et al. (1991) first proposed a relativistic model for pulsar polarization by incorporating the rotation effect, and predicted the phase lag between the centers of the PA curve and the profile. The rotation also influences the intensities of the leading and trailing components of the profile (Blaskiewicz et al. 1991; Thomas & Gangadhara 2007). Dyks et al. (2010) analyzed the rotation and found two competing effects: the enhancement of the trailing side caused by aberration and retardation (AR) and the weakening of the trailing side caused by the rotation-induced asymmetry of curvature radius. In the pioneer paper, Blaskiewicz et al.

^{*} E-mail: pfwang@nao.cas.cn

(1991) calculated only the emission of particles with velocity pointing towards the observer, and did not consider the emissions from particles of nearby field lines, which may still beam towards us. Meanwhile, the influence of rotation on polarization intensities are not taken into account. Gangadhara (2010) considered the emission from all nearby field lines, but did not incorporate the rotation in his detailed work.

In this paper, we study the curvature radiation in the rotating pulsar magnetosphere. The curvature emission of single particle and a bunch of particles streaming along the magnetic field lines are calculated using numerical simulations. The paper is organized as following. In Section 2, we present the details of our calculation for the emission from a single relativistic particle. In Section 3 the rotation distorted patterns of curvature emission are calculated for the emission cone at a given height. The polarization profiles from a given height are calculated for three typical density models in the form of core, cone and patches for various emission geometries. The polarized profiles from the whole magnetosphere are presented in Section 4. Our conclusions are given Section 5.

2 CURVATURE RADIATION OF A SINGLE PARTICLE IN ROTATING PULSAR MAGNETOSPHERE

The pulsar magnetosphere consists of relativistic plasma streaming along magnetic field lines. The magnetic field is generally thought to be an inclined dipole, which is given by

$$\mathbf{B} = B_* \left(\frac{R_*}{r}\right)^3 [3\hat{\mathbf{r}}(\hat{\mathbf{r}} \cdot \hat{\mathbf{m}}) - \hat{\mathbf{m}}], \quad (1)$$

where B_* is the surface magnetic field, R_* is the neutron star radius, $\hat{\mathbf{r}}$ is the unit vector along \mathbf{r} , and $\hat{\mathbf{m}}$ represents the unit vector for the magnetic dipole moment. Curvature radiation is generated when relativistic charged particles (electrons or positrons) streaming along the curved field lines, the electric field from a single particle is

$$\mathbf{E}(t) = \frac{\mathbf{n} \times [(\mathbf{n} - \mathbf{v}) \times \mathbf{a}]}{(1 - \mathbf{n} \cdot \mathbf{v})^3}, \quad (2)$$

with \mathbf{n} the wave vector unity, \mathbf{v} the particle velocity and \mathbf{a} the acceleration. In previous studies of curvature radiation in pulsar magnetospheres (Benford & Buschauer 1977; Gangadhara 2010), the rotation of magnetosphere is usually neglected, thus the particle velocity \mathbf{v} is simply parallel to the tangential direction of the \mathbf{B} field at the emission point, and the acceleration \mathbf{a} is in the same \mathbf{B} field line plane as the emission point. However, the co-rotation of a particle with the magnetosphere changes \mathbf{v} and \mathbf{a} , and affects the intensity and polarization of the particle emission significantly (Blaskiewicz et al. 1991). In this section, we discuss the correction to the particle velocity and acceleration in detail, and give a precise equation to calculate the curvature radiation of a single particle in rotating pulsar magnetosphere.

2.1 The particle velocity, acceleration and emission location

In the co-rotating frame, the relativistic particles or bunches are streaming along the open magnetic field lines with a velocity of

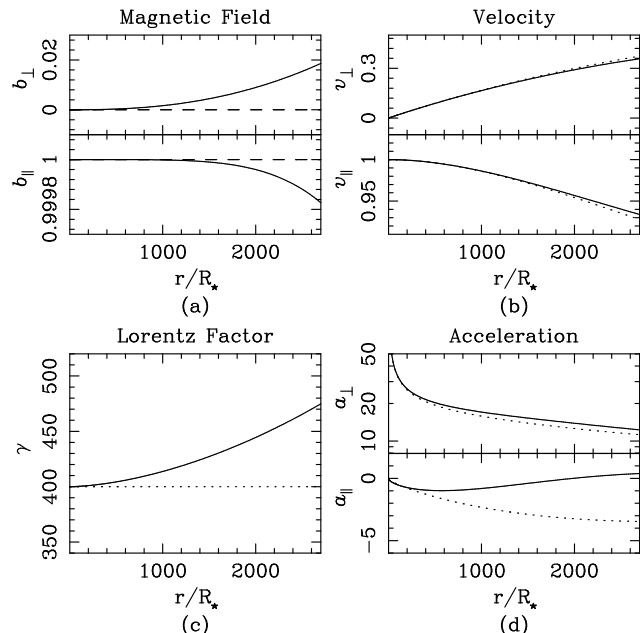


Figure 1. The modified magnetic field direction, velocity, Lorentz factor and acceleration of the particles along the last open field line considering the co-rotation of pulsar magnetosphere. Fig. (a) shows the magnetic field directions in the fixed lab frame (solid line) and the co-rotating frame (dashed line). In Fig. (b), (c) and (d), the solid lines show the precise relativistic velocity, Lorentz factor and acceleration given by equation (4) and (7), the dotted lines are approximations given by equations (5) and (8). Our calculation chooses the last open field line, which is in a plane with azimuthal angle of -10° . The other parameters involved in calculation are $P = 1$ s, $\alpha = 70^\circ$, and $\gamma = 400$.

$$\mathbf{v}' = v' \hat{\mathbf{b}}' \quad (3)$$

here $\hat{\mathbf{b}}' = \mathbf{B}/|\mathbf{B}|$ is a unit vector along the tangent direction of the magnetic field line, v' is the velocity magnitude in terms of light speed c . The particles also experience rotation with velocity $\mathbf{v}_r = \boldsymbol{\Omega} \times \mathbf{r}/c$. In the lab frame, the total velocity \mathbf{v} should be the addition of \mathbf{v}' with \mathbf{v}_r by Lorentz transformation, which reads

$$\mathbf{v} = \frac{\mathbf{v}' + \frac{(\gamma_r - 1)}{v_r^2} (\mathbf{v}_r \cdot \mathbf{v}') \mathbf{v}_r + \gamma_r \mathbf{v}_r}{\gamma_r (1 + \mathbf{v}_r \cdot \mathbf{v}')} \quad (4)$$

here v_r is the magnitude for the rotation velocity. Its corresponding Lorentz factor is $\gamma_r = 1/\sqrt{1 - v_r^2}$. Equation (4) gives the precise particle velocity in the lab frame. **The velocity \mathbf{v} can also be written as**

$$\mathbf{v} = \kappa \hat{\mathbf{b}} + \boldsymbol{\Omega} \times \mathbf{r}/c. \quad (5)$$

Here, κ is the function of v and v_r , $\hat{\mathbf{b}}$ denotes the magnetic field direction in the fixed lab frame, which is the Lorentz transformation of $\hat{\mathbf{b}}'$. The difference between $\hat{\mathbf{b}}$ (solid line) and $\hat{\mathbf{b}}'$ (dashed line) is very small for a low emission height ($r < 500R_*$) as shown in Fig. 1 (a). Therefore, most of the previous studies (Blaskiewicz et al. 1991; Kumar & Gangadhara 2012) can ignore the difference and use $\hat{\mathbf{b}}'$ instead of $\hat{\mathbf{b}}$ in equation (5). In Blaskiewicz et al. (1991), κ is

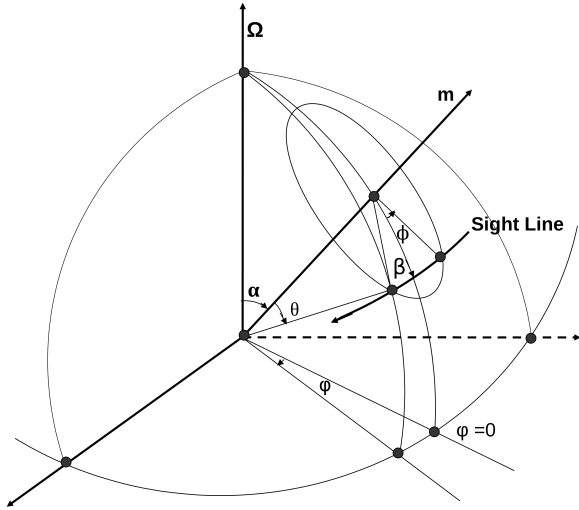


Figure 2. The coordinates for pulsar emission geometry. Ω represents the rotation axis, \mathbf{m} is the dipole moment. The magnetic inclination angle is α with respect to Ω . Sight line has impact angle of β , cutting the beam. The rotation phase is $\varphi = \Omega t$ starting from the $\Omega - \mathbf{m}$ plane. The magnetic polar and azimuthal angles are θ and ϕ .

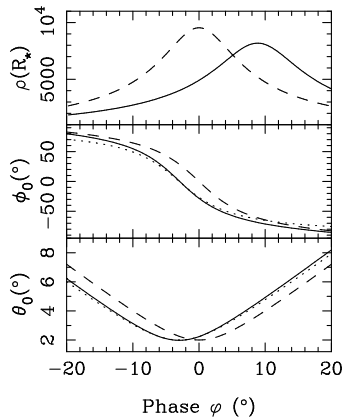


Figure 3. Tangential emission points (magnetic polar angle θ_0 and azimuth angle ϕ_0) and the corresponding curvature radii ρ for various rotation phases, φ . The dashed lines represent the case without rotation, while the solid lines are the results by taking the rotation into account. The dotted lines show the results given by Blaskiewicz et al. (1991). The parameters used for calculation are $P = 1\text{ s}$, $\alpha = 30^\circ$, $\beta = 3^\circ$, $\gamma = 400$, $r = 250R_*$.

limited to be a constant, since they just consider the emission from low heights where v_r is very small. To coordinate the total velocity with the light speed, Gangadhara (2005) introduced the evolvement of κ with height by assuming the Lorentz factor to be a constant, as shown with the dotted line Fig. 1(c). However, according to equation (4), the Lorentz factor for the particle is changing with height shown by the solid line in Fig. 1(c). The precise relativistic velocity given by equation (4) and the approximation are shown in Fig. 1(b). Within several hundred of R_* , the difference is very small.

The radiation of a relativistic particle is beamed in its velocity direction $\hat{\mathbf{v}}$. It requires the alignment between the wave vector unity \mathbf{n} and $\hat{\mathbf{v}}$ for the observer to receive considerable radiation. At a given emission height, the emission location (θ_0, ϕ_0) at each rotation phase φ (see Fig. 2) can be determined by solving $\mathbf{n} = \hat{\mathbf{v}}$, which is the tangential point of the trajectory along the line of sight. Here (θ_0, ϕ_0) is the polar coordinate of magnetic axis, with $\phi_0 = 0$ corresponding to the $\Omega - \mathbf{m}$ plane. Blaskiewicz et al. (1991) has done similar calculations by analytically solving $\mathbf{n} = \kappa \hat{\mathbf{b}} + \Omega \times \mathbf{r}/c$. Our numerical calculations develop their results further to higher magnetosphere using equation (4). The emission locations from our calculation are shown in Fig. 3, which is very close to that given by Blaskiewicz et al. (1991). Rotation demonstrates its effect by shifting the emission locations towards an early phase.

The particle acceleration is also affected by the co-rotation with pulsar magnetosphere. The charged particle streams along the magnetic field line, whose trajectory is described by $r = r_e \sin^2 \theta$ in the co-rotating magnetic axis frame. Here r_e is the field line constant, θ is the polar angle from the magnetic axis. The particle acceleration in the co-rotating frame reads

$$\mathbf{a}' = \frac{v'^2 c}{|\mathbf{b}'|} \frac{\partial \hat{\mathbf{b}}}{\partial \theta} \quad (6)$$

here $\mathbf{b} = \partial \mathbf{r} / \partial \theta$ is the magnetic field line tangent and its magnitude $|\mathbf{b}| = (r_e / \sqrt{2}) \sin \theta \sqrt{5 + 3 \cos(2\theta)}$. The acceleration in the lab frame can be calculated by

$$\mathbf{a} = \frac{d\mathbf{v}}{dt}. \quad (7)$$

Substitute the approximation of \mathbf{v} (equation 5) in the above equation, we have

$$\mathbf{a} = \frac{\kappa^2 c}{|\mathbf{b}|} \frac{\partial \hat{\mathbf{b}}}{\partial \theta} + \frac{\kappa c}{|\mathbf{b}|} \frac{\partial \kappa}{\partial \theta} \hat{\mathbf{b}} + 2\kappa \Omega \times \hat{\mathbf{b}} + \Omega \times (\Omega \times \mathbf{r}/c), \quad (8)$$

which is equivalent to equation (7) in Kumar & Gangadhara (2012). Substitute the precise velocity equation (4) in equation (7), we can also obtain the analytic equation of \mathbf{a} without approximation, which is too complicated to write done here. The numerical results for the precise acceleration from Lorentz transformation and the approximated one given by equation (8) are shown in Fig. 1(d). The approximated treatment for the acceleration remains good only at low emission height of several hundred R_* , but becomes significantly different from the precise acceleration at outer magnetosphere.

The curvature radius of the particle trajectory in the lab frame is approximately given by $\rho \simeq cv^2/a$. In the upper panel of Fig. 3, we calculated the curvature radii for the trajectories at each rotation phase using the acceleration. The leading side tends to have smaller curvature radius compared to the case without rotation, while the trailing side behaves in the opposite way. Thomas & Gangadhara (2007) pointed out that the rotation induces a significant curvature into the particle trajectories, which are deflected towards the rotation direction. The magnitude of the deflection on leading side becomes larger compared with the no-rotating case, while the deflection on the trailing side is weakened. Our results is consistent with Thomas & Gangadhara (2007). The modifications of particle velocity, acceleration and emission

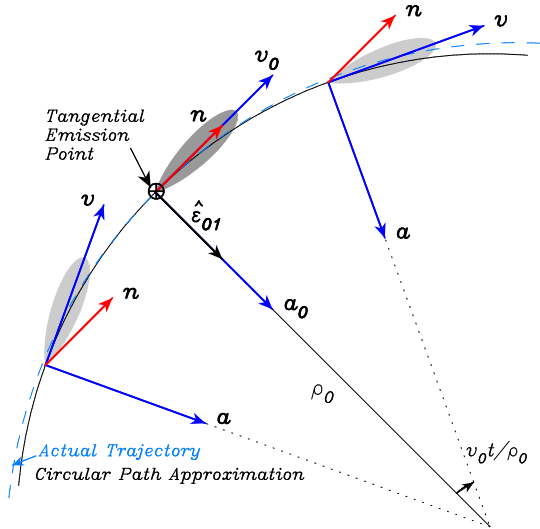


Figure 4. The circular path approximation (solid curve) to the actual particle trajectory (dashed curve). At the tangential emission point, the particle velocity \mathbf{v}_0 is parallel to the line of sight \mathbf{n} .

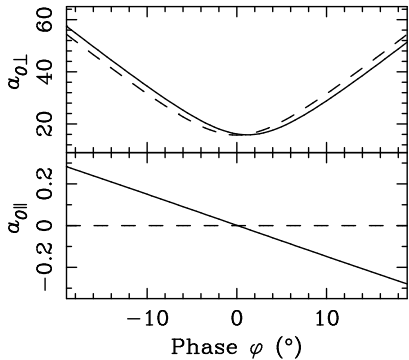


Figure 5. The components of acceleration at each emission point parallel and perpendicular to the velocity direction. The solid lines are for the corrected acceleration including the rotation effect, while the dashed lines are drawn without considering the rotation. The parameters used here are $P = 1$ s, $\alpha = 30^\circ$, $\beta = 3^\circ$, $\gamma = 400$, $r = 50R_*$.

location due to the co-rotation of particles with pulsar magnetosphere have significant roles on pulsar radiation property, which will be discussed in Section 3.

2.2 Curvature Emission from a single particle

Knowing the particle velocity, acceleration and emission location of the relativistic particle, we can directly calculate its curvature radiation fields. Note that according to equation (2), the emission location, where $\mathbf{n} \cdot \hat{\mathbf{v}} = 1$, is the point where the radiation electric field is the strongest. Before and after this point within the angle of $1/\gamma$, the particle still emits in the direction of \mathbf{n} but the magnitude of the electric field becomes weakened (see Fig. 4). The total electric field emitted from this particle should be the coherent integration of the emission from the whole trajectory, especially near the tangential emission point.

To study the emission from a relativistic particle, we set

up a reference frame $(\hat{\mathbf{e}}_{01}, \hat{\mathbf{e}}_{02}, \hat{\mathbf{v}}_0)$ at the tangential point along the line of sight in the instantaneous trajectory plane, shown in Fig. 4. Here the subscript "0" stands for the parameters at the tangential point, \mathbf{v}_0 and \mathbf{a}_0 are the velocity and acceleration at the tangential point, $\hat{\mathbf{v}}_0$ is the unit vector along \mathbf{v}_0 . The other two axes of the frame are described as

$$\begin{aligned}\hat{\mathbf{e}}_{01} &= \hat{\mathbf{e}}_{02} \times \hat{\mathbf{v}}_0, \\ \hat{\mathbf{e}}_{02} &= \frac{\hat{\mathbf{v}}_0 \times \hat{\mathbf{a}}_0}{|\hat{\mathbf{v}}_0 \times \hat{\mathbf{a}}_0|},\end{aligned}\quad (9)$$

$\hat{\mathbf{e}}_{01}$ is in the \mathbf{v}_0 - \mathbf{a}_0 plane and almost parallel to \mathbf{a}_0 , and $\hat{\mathbf{e}}_{02}$ is perpendicular to the plane. In Fig. 5, we compare the two orthogonal components of \mathbf{a}_0 along $\hat{\mathbf{v}}_0$ ($\mathbf{a}_{0\parallel}$) and $\hat{\mathbf{e}}_{01}$ ($\mathbf{a}_{0\perp}$), and find $|\mathbf{a}_{0\parallel}|/|\mathbf{a}_{0\perp}| \lesssim 10^{-2}$ for various particle trajectories at the corresponding pulsar rotation phases. This means that the contribution of $\mathbf{a}_{0\parallel}$ to the total emission can be neglected. It was pointed out by Jackson (1975) that the radiation emitted by an extremely relativistic particle subject to arbitrary accelerations is equivalent to that by a particle moving on an appropriate circular path. The approximate circular path around the tangential point for the particle trajectory has a radius of curvature of

$$\rho_0 = c \frac{v^2}{|\mathbf{a}_0|}, \quad (10)$$

here we suppose $\hat{\mathbf{a}}_0 \simeq \mathbf{a}_{0\perp}$, since $|\mathbf{a}_{0\parallel}| \ll |\mathbf{a}_{0\perp}|$. The velocity and acceleration of the bunch in the vicinity of the tangential point can be expressed by

$$\begin{aligned}\mathbf{v} &= |\mathbf{v}_0| \left[\cos\left(\frac{v_0 t}{\rho_0}\right) \hat{\mathbf{v}}_0 + \sin\left(\frac{v_0 t}{\rho_0}\right) \hat{\mathbf{e}}_{01} \right], \\ \mathbf{a} &= |\mathbf{a}_0| \left[-\sin\left(\frac{v_0 t}{\rho_0}\right) \hat{\mathbf{v}}_0 + \cos\left(\frac{v_0 t}{\rho_0}\right) \hat{\mathbf{e}}_{01} \right].\end{aligned}\quad (11)$$

The position vector for the particle in the circular path reads

$$\mathbf{r}_{\text{cir}} = -\rho_0 \hat{\mathbf{a}}, \quad (12)$$

with $\hat{\mathbf{a}} = \mathbf{a}/|\mathbf{a}|$. The radiating electric field of the relativistic particle at frequency ω in direction \mathbf{n} is the Fourier Transform of $\mathbf{E}(t)$, which is governed by

$$\mathbf{E}(\omega) = \frac{q e^{i\omega R_0/c}}{\sqrt{2\pi} c R_0} \int_{-\infty}^{\infty} \frac{\mathbf{n} \times [(\mathbf{n} - \mathbf{v}) \times \mathbf{a}]}{(1 - \mathbf{n} \cdot \mathbf{v})^2} e^{i\omega(t - \mathbf{n} \cdot \mathbf{r}_{\text{cir}}/c)} dt, \quad (13)$$

here, R_0 is the distance between the circular path center and the observer.

We should note that the integration in equation 13 is highly oscillating and not easy to integrate. Following Gangadhara (2010), we expand the integrand to the third order around $t = 0$ and then get the analytic expression of the integration. The total integration can then be calculated directly from the analytic equation. The detailed description of this method is given in the Appendix B of Gangadhara (2010).

In our calculation, we use the assumption of a circular path to describe the trajectory of the relativistic particles around the tangential emission point. To demonstrate its feasibility, we further compare in Fig. 6 the integrand term in equation (13) near the tangential emission point using actual trajectory, **similarly done by Kumar & Gangadhara (2012)** and circular path approximation. The magnitude of the integrand is highly oscillating when the particle is away

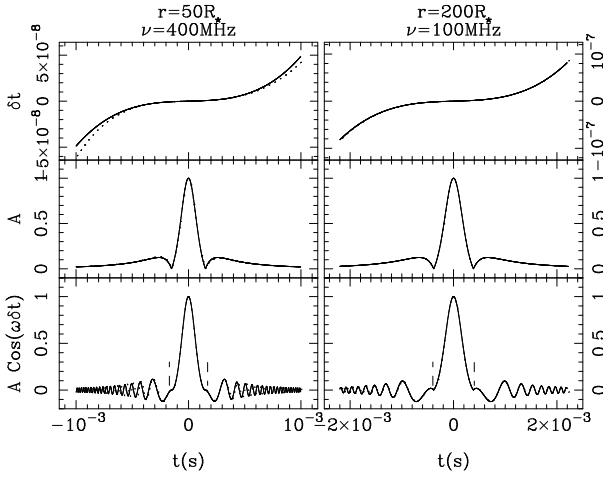


Figure 6. The integrand term in equation (13) near the tangential emission point (where $t = 0$ s) considering the co-rotation of the particle with pulsar magnetosphere. Here $A = |\mathbf{n} \times [(\mathbf{n} - \mathbf{v}) \times \mathbf{a}] / (1 - \mathbf{n} \cdot \mathbf{v})^2|$, $\delta t = t - \mathbf{n} \cdot \mathbf{r}_{\text{cir}} / c$, and $A \cos(\omega \delta t)$ are the magnitude of the integrand. The dotted lines are for the actual trajectory of the particle in the meridional plane, while the solid lines present the results using the circular path approximation. The left and right panels show the results for lower and higher emission radius (and corresponding frequencies), respectively. The other parameters used for calculation here are $P = 1$ s, $\alpha = 10^\circ$, $\beta = 3^\circ$ and $\gamma = 400$.

from the tangential emission point about $|t| > 4 \times 10^{-4}$ s (or about $10R_*$), so that the integration outside is almost vanished due to the oscillation. The central part near $t = 0$ between the two dashed lines in the figure dominates the result of integration. In this central part, the difference by using the assumed circular path and the ideal trajectory is negligible. Therefore, the electrical fields calculated from the circular path approximation are accurate enough but much easier.

The observed emission is the transverse component of the electric field perpendicular to the line of sight \mathbf{n} . We have to transform the calculated $\mathbf{E}(\omega)$ to the lab frame XYZ , with \mathbf{Z} along the line of sight \mathbf{n} , and $\mathbf{\Omega}$ in the XZ plane. The Stokes parameters are defined as follows

$$\begin{aligned} I &= E_X E_X^* + E_Y E_Y^*, \\ Q &= E_X E_X^* - E_Y E_Y^*, \\ U &= 2\text{Re}[E_X^* E_Y], \\ V &= 2\text{Im}[E_X^* E_Y]. \end{aligned} \quad (14)$$

2.3 Pulse profile of curvature emission from a single particle

Previously, only the radiation exactly along the velocity direction of the relativistic particle is considered for the pulsar profile. It means that only the radiation by a particle at (θ_0, ϕ_0) with a velocity towards the observer contributes to the observed intensity at a given rotation phase. Using equation (13), we can calculate the polarized emission from a single particle at various phases to get the intensity and polarization profiles, as is shown in Fig. 7. The results are very similar to those given by Blaskiewicz et al. (1991), where they use the total emission of the particle in the emission

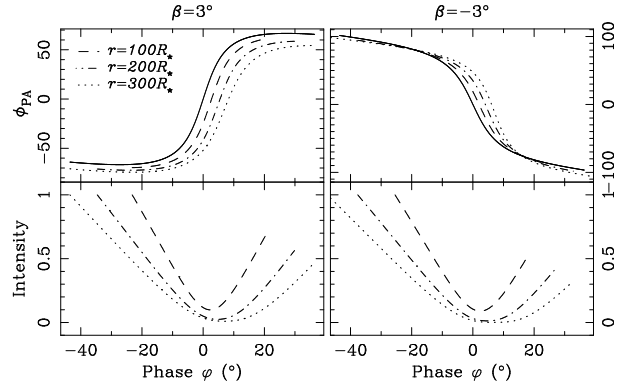


Figure 7. Pulse profiles of intensity and position angles emitted from a single particle at the tangential emission point at various rotation phase. The calculation is made for different heights $r = 100R_*$, $200R_*$ and $300R_*$. The solid line presents the PA profile without rotation. The other parameters used here are $P = 1$ s, $\alpha = 30^\circ$ and $\gamma = 400$.

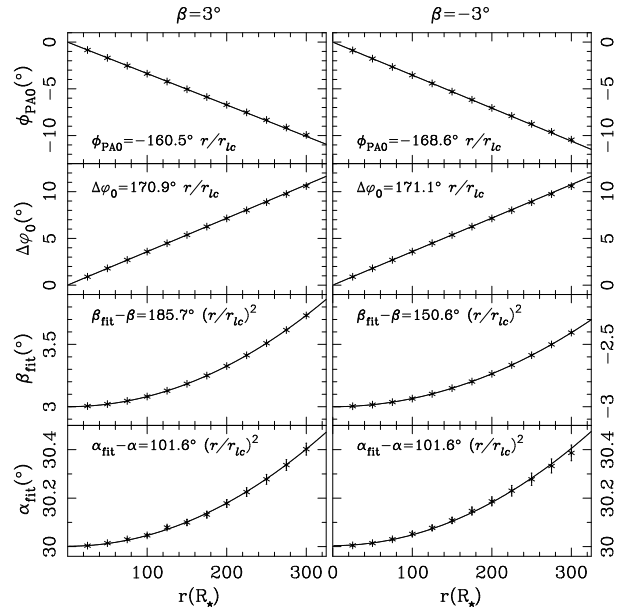


Figure 8. The fitted parameters α_{fit} , β_{fit} , $\Delta\phi_0$ and $\phi_{\text{PA}0}$ vary with emission heights. The dots are the values by fitting the PA profiles shown in Fig. 7 with the rotating vector model (equation 15). The solid lines present the best fit to the dots, which is described by the equations given in each panel.

cone at the tangential point instead of the integration along the trajectory. The emission is almost 100% linearly polarized since the emission at each phase comes from a single particle. The leading part of the intensity profile is brighter than the trailing side because of the rotation induced curvature for the particle trajectory. The most obvious are the polarization position angle curves shifted towards a later phase due to the aberration effect.

The shift of a PA profile caused by rotation is larger at a larger emission height due to the relatively larger rotation velocity $\mathbf{\Omega} \times \mathbf{r}$. To show the shifts varying with the emission heights, we can fit the shifted PA curves at different heights

by using the rotating vector model (Komesaroff et al. 1970)

$$\tan(\phi_{\text{PA}} - \phi_{\text{PA}0}) = \frac{\sin(\varphi - \Delta\varphi_0) \sin \alpha}{\sin(\alpha + \beta) \cos \alpha - \cos(\alpha + \beta) \sin \alpha \cos(\varphi - \Delta\varphi_0)}. \quad (15)$$

Here $\phi_{\text{PA}0}$ describes the PA profile shift along the perpendicular direction in Fig. 7, $\Delta\varphi_0$ represents the phase shift of a PA profile. Evolution of the four fitting parameters (α_{fit} , β_{fit} , $\Delta\varphi_0$ and $\phi_{\text{PA}0}$) with height are shown in Fig. 8. Rotation induced aberration not only delays the polarization sweep with positive $\Delta\varphi_0$, but also shifts the entire PA sweep downward with negative $\phi_{\text{PA}0}$ (Hibschan & Arons 2001). Both of these shifts ($\phi_{\text{PA}0}$ and $\Delta\varphi_0$) are the first order functions of r . Pulsar emission geometry is also distorted by the rotation, since the fitting values of α_{fit} and β_{fit} change with heights. PA curves are steepened for $\beta < 0$ but flattened for $\beta > 0$ (Blaskiewicz et al. 1991). The fitting value of the dipole inclination angle α_{fit} increases with r . The influences of rotation on α_{fit} and β_{fit} determination are both second order functions of r , as $\beta_{\text{fit}} - \beta \propto r^2$ and $\alpha_{\text{fit}} - \alpha \propto r^2$.

3 CURVATURE RADIATION AT A GIVEN HEIGHT

A relativistic particle streaming along a magnetic field line in magnetosphere will emit in a cone of $1/\gamma$ around its velocity direction. Thus the observed emission at a pulsar rotation phase comes from the particles not only along one magnetic field line with $\mathbf{n} \cdot \hat{\mathbf{b}} = 1$, but also the nearby field lines within the $1/\gamma$ emission cone. In this section, we will calculate the curvature radiation from the particles at a given height steaming along a bunch of magnetic field lines.

3.1 Emission pattern at a given height

The emission received at one rotation phase actually contains the contributions from all nearby field lines around the tangential emission point at a given height. Fig. 9 shows the emission patterns for the polarized emission with or without rotation at different heights and impact angle β . The patterns are plotted in the coordinates (θ, ϕ) around the magnetic axis for different rotation phases. The central point of the patterns corresponds to the tangential point where the velocity aligns with the line of sight. The patterns extend to approximately 0.15° in magnetic polar angle θ , and about 2° – 4° in magnetic azimuth ϕ , which agree with the $1/\gamma$ emission cone since we take $\gamma = 400$. The total intensity I distributes in an ellipse manner around the central maximum. The linear polarization L has almost the same patterns as I but with smaller magnitudes. The circular polarization V is shown in two antisymmetrical lobes with + and – signs corresponding to the left and right hands, with the maximum intensity of V as about 20% of the peak total intensity.

Our calculations in Fig. 9 make it clear that the rotation systematically distorts the emission patterns compared with the case without rotation in which the long axes of I and L beams and the zero line of the V are all vertically aligned. Since particles at a larger emission height have comparatively larger rotation velocity and hence trajectories are much more bent. For the emission from higher radii, the

Table 1. The sign of the net circular polarization of particle emission for various density gradient at an emission height of $50R_\star$.

	$\beta > 0$	$\beta < 0$
$\partial N/\partial\theta > 0$	–	+
$\partial N/\partial\theta < 0$	+	–
$\partial N/\partial\phi > 0$	+	+
$\partial N/\partial\phi < 0$	–	–

distortion of beam pattern due to rotation becomes more serious. The beam patterns for opposite impact angles (see Fig. 9a and 9d for $\pm\beta$) are almost the same except for the opposite signs in the V patterns. The beam pattern for a smaller impact angle β tends to have large distortion (see Fig. 9f), because the rotation induced acceleration is more dominating for the particles in the field lines near the magnetic axis, compared to the curvature acceleration. Note that the beam patterns for the phases with opposite signs, i.e., $\varphi = \pm 5^\circ$ or $\pm 10^\circ$, are asymmetric. The strongest distortion happens at a late phase ($\varphi > 0^\circ$), because the rotation bends the trajectories towards the rotating direction. The long axes of the beam patterns for an extremely high emission radii, i.e., $r \sim 400R_\star$ or higher, are rotated by more than 90° compared those without rotation.

3.2 Polarization profiles for the emission from a given height

The observed Stokes parameters at each rotation phase are the integration of all visible beam patterns from all particles in all field lines. It is generally believed that pulsar radiations are coherent, and the width of the coherent bunches in the θ - ϕ plane should be much smaller than the radiating wavelength for the coherency to be efficient. The typical size of the $1/\gamma$ emission pattern at a given height is much larger than the coherent width. Therefore, the emission at a given height should be added incoherently, which reads

$$\begin{aligned} I_r &= \int_{\theta_0 - \delta\theta}^{\theta_0 + \delta\theta} \int_{\phi_0 - \delta\phi}^{\phi_0 + \delta\phi} N(r, \theta, \phi) I r^2 \sin\theta d\theta d\phi, \\ Q_r &= \int_{\theta_0 - \delta\theta}^{\theta_0 + \delta\theta} \int_{\phi_0 - \delta\phi}^{\phi_0 + \delta\phi} N(r, \theta, \phi) Q r^2 \sin\theta d\theta d\phi, \\ U_r &= \int_{\theta_0 - \delta\theta}^{\theta_0 + \delta\theta} \int_{\phi_0 - \delta\phi}^{\phi_0 + \delta\phi} N(r, \theta, \phi) U r^2 \sin\theta d\theta d\phi, \\ V_r &= \int_{\theta_0 - \delta\theta}^{\theta_0 + \delta\theta} \int_{\phi_0 - \delta\phi}^{\phi_0 + \delta\phi} N(r, \theta, \phi) V r^2 \sin\theta d\theta d\phi. \end{aligned} \quad (16)$$

Here $N(r, \theta, \phi)$ serves as particle density distribution function, the half-width $\delta\theta$ and $\delta\phi$ of the emission pattern are chosen to be 0.1° and 2° to cover the pattern of the emission cone. For simplicity we assume that the density distributions across r , θ and ϕ are independent, i.e., $N(r, \theta, \phi) = n(r)f(\theta)g(\phi)$. The density variation along the height $n(r) \propto r^{-3}$, and $n(r)$ is a constant for a given emission height.

If the particle density, N , keeps constant in all field lines at a given height, the observed circular polarization should

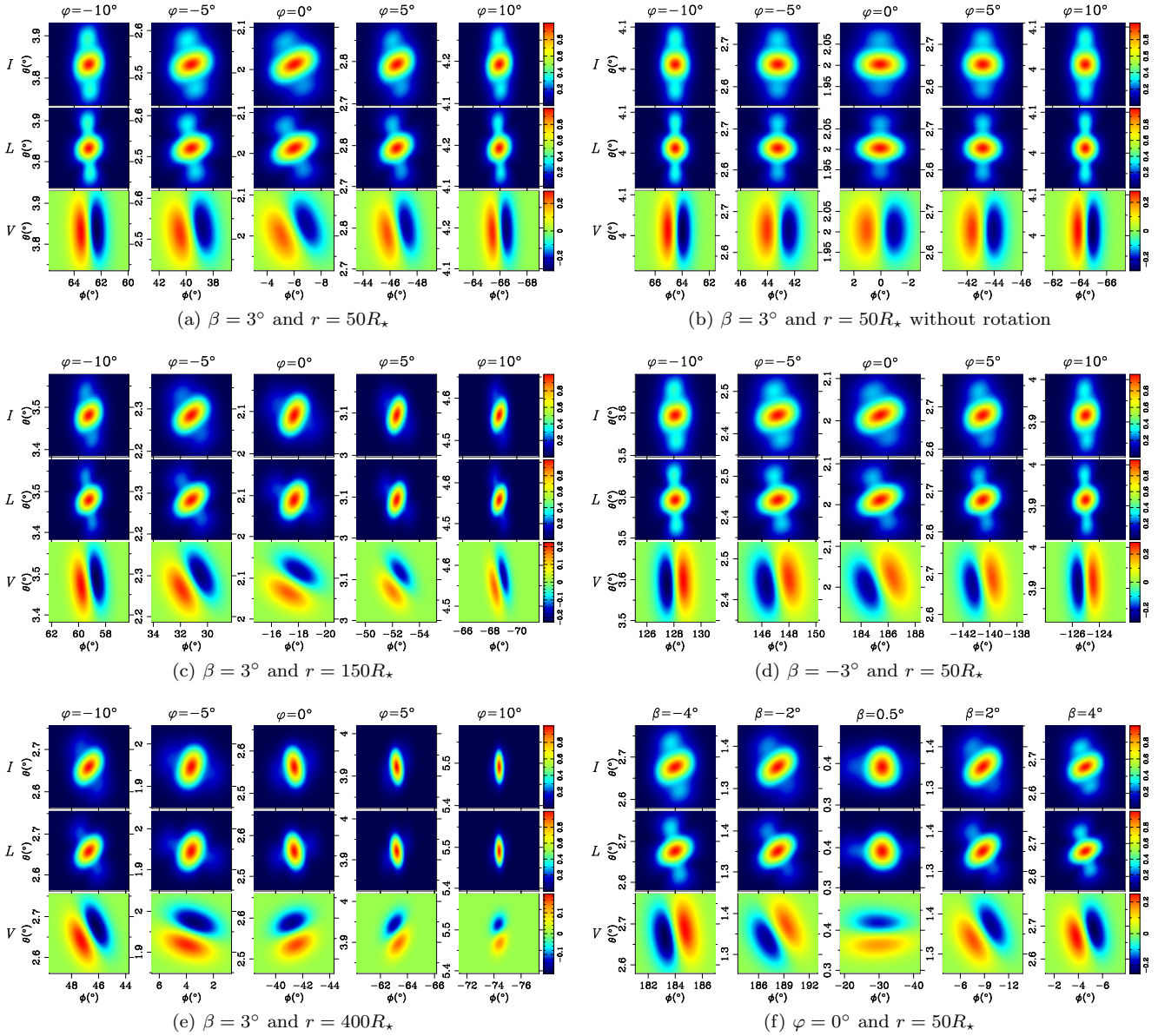


Figure 9. Emission patterns for the total intensity I , linear polarization L and circular polarization V around the tangential emission point calculated for various heights and β at different rotation phases ($\varphi = 0^\circ, \pm 5^\circ, \pm 10^\circ$). The patterns without rotation are always similar for different r and β , so that we just show one for $r = 50R_*$ and $\beta = 3^\circ$. The two axes for plots are the magnetic polar angle θ and azimuth angle ϕ . The other parameters used for calculations are $P = 1$ s, $\alpha = 30^\circ$, $\gamma = 400$ and $\nu = \omega/2\pi = 400$ MHz.

be zero in all the cases since it is always symmetrical with the central point, and the integrations of particle emission from many field lines will smear out the circular polarization. However, in most cases the density distribution across field lines are not uniform. Modulation of N across θ and ϕ may result in net circular polarization. For example, in the case without rotation in Fig. 9b, the pattern of V is symmetric with respect to ϕ , so that only the density gradient along ϕ can produce net V , while the density gradient along θ can not. The detailed discussion for this case can be found in Gangadhara (2010). In the cases of rotation, the observed beam patterns become complicated due to the distortion. The circular polarization depends on the density gradients along θ and ϕ , following the rule shown in Table 1 for the

emission from a typical emission height $r = 50R_*$ (see Fig. 9a and f).

3.2.1 Cone-core model

The observation of pulsar mean profiles suggested a classical pulsar beam model with a central core surrounded by one or multiple hollow cones (Backer 1976; Rankin 1993). These cone-core regions in pulsar magnetosphere are filled with relativistic particles streaming along the open magnetic field lines, which is generated by sparking process on neutron star polar cap (Ruderman & Sutherland 1975). We explore the emission profile for the particle density distributions in the form of core and cone in the polar cap region streaming

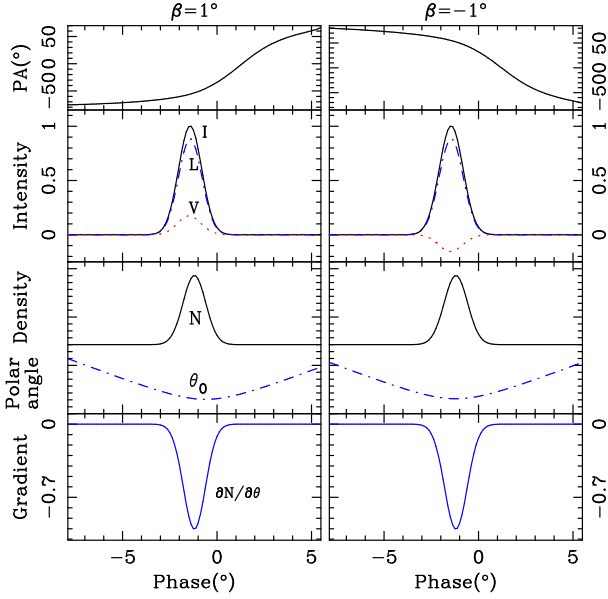


Figure 10. Polarization profiles (I , L , V and PA) at 400 MHz from a height of $50R_*$ for the core density distribution. The solid, dash-dotted and dotted lines represent I , L and V , respectively. The density N , magnetic polar angle, θ , and the density gradient $\partial N/\partial\theta$ vary with the rotation phase ϕ . The left and right panels are plotted for opposite impact angles $\beta = \pm 1^\circ$. The other parameters used here are $P = 1s$, $\alpha = 30^\circ$, $\gamma = 400$ and $\sigma_{\theta_*} = 0.0005$.

out from the neutron star surface and extending to high magnetosphere.

The core density distribution is written as

$$f(\theta) = f_0 \exp\left(-\frac{\theta_*^2}{2\sigma_{\theta_*}^2}\right),$$

$$g(\phi) = 1. \quad (17)$$

Here f_0 is the maximum density, θ_* is the polar angle of a field line footed on the neutron star surface in the polar cap region, σ_{θ_*} is the characteristic width of the gaussian distribution on the star surface. The polarized profiles from particles distributed in this core at a height of $r = 50R_*$ are shown in Fig. 10. Due to rotation, the ‘‘S’’ shaped PA curve is shifted towards a later phase, while the intensity curve to an earlier phase, as predicted by Blaskiewicz et al. (1991). Single sign of circular polarization is generated because of the density gradient along θ . In the case of positive β (see the left panels of Fig. 10), the left hand CP ($V > 0$) is generated because $\partial N/\partial\theta < 0$ for all phases, but the right hand CP for negative β (see the right panels of Fig. 10). Both of them agree well with Table 1. The core density model always has $\partial N/\partial\theta < 0$ and $\partial N/\partial\phi = 0$, so that the net CP always has a single sign for all rotation phases.

The cone density distribution reads

$$f(\theta) = f_0 \exp\left[-\frac{(\theta_* - s\theta_{*lof})^2}{2\sigma_{\theta_*}^2}\right],$$

$$g(\phi) = 1. \quad (18)$$

Here $\theta_{*lof} = \sin^{-1}(\sqrt{R_*/r_{e,lof}})$ is the polar angle maximum on the star surface corresponding to the last open field line, the dimensionless parameter s describes the peak position for the maximum density in terms of θ_{*lof} . The two sets

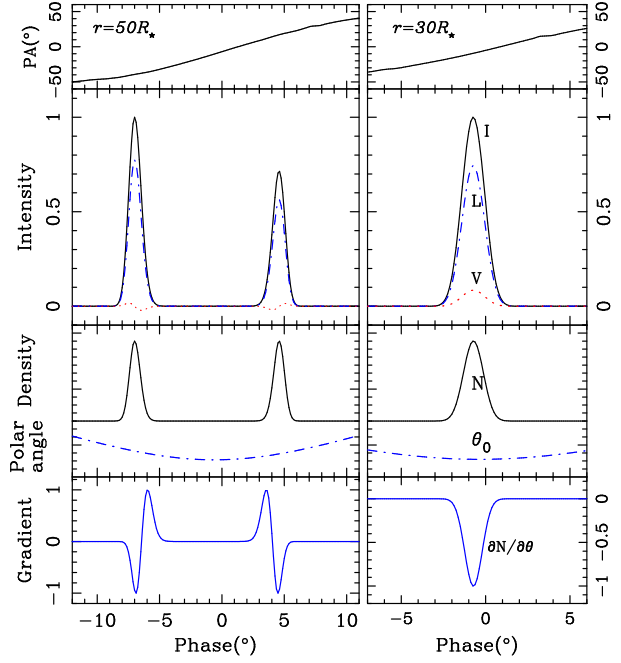


Figure 11. Same as Fig. 10 but for the density distribution in the form of a cone. Left and right panels stand for the emission profiles from $30R_*$ and $50R_*$, respectively. The other parameters used here are $P = 1s$, $\alpha = 30^\circ$, $\beta = 5^\circ$, $\gamma = 400$, $\sigma_{\theta_*} = 0.0002$ and $s = 0.7$.

of polarized profiles for the cone density model are shown in Fig. 11 with the same impact angle of $\beta = 5^\circ$ but two different emission heights. For a higher emission radius of $r = 50R_*$ (left panels), the line of sight cuts through the density cone close to the magnetic axis, which results in double intensity components. For each component, $\partial N/\partial\theta$ changes signs, which results in the sign reversal of circular polarization. The opposite $\partial N/\partial\theta$ variation causes the opposite sign reversals of V . For a lower emission height of $r = 30R_*$ (right panels), sight line will cut across the edge part of the density cone. Therefore only one component can be observed. The density gradient $\partial N/\partial\theta < 0$, so that the circular polarization has one sign across the pulse phases, very similar as the case of core emission.

3.2.2 Patch model

The patch density model describes the different density components randomly distributed within the open field line area. The patch foots located on the neutron star surface in the polar cap region can be described as

$$f(\theta) = f_0 \exp\left[-\frac{(\theta_* - s\theta_{*lof})^2}{2\sigma_{\theta_*}^2}\right],$$

$$g(\phi) = g_0 \exp\left[-\frac{(\phi - \phi_p)^2}{2\sigma_\phi^2}\right]. \quad (19)$$

Here g_0 is the maximum density constant similar to f_0 , ϕ_p is the peak position of a density patch in the magnetic azimuth direction, and σ_ϕ is the corresponding characteristic width. We do not use the subscript ‘‘*’’ for ϕ and ϕ_p , because they do not change with the height.

The position of a patch ($s\theta_{*lof}$, ϕ_p) affects the density

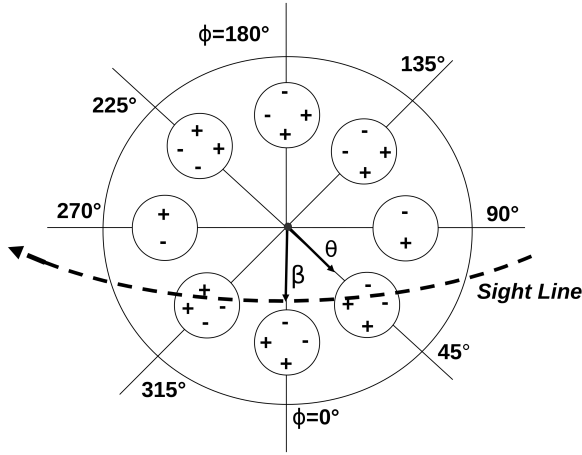


Figure 12. Sketch map of the discussed patches in the open field line region. The signs of “+” and “-” in the patches represent the signs of circular polarization at a height of $50 R_*$. See detailed profiles in Fig. 13 and 14.

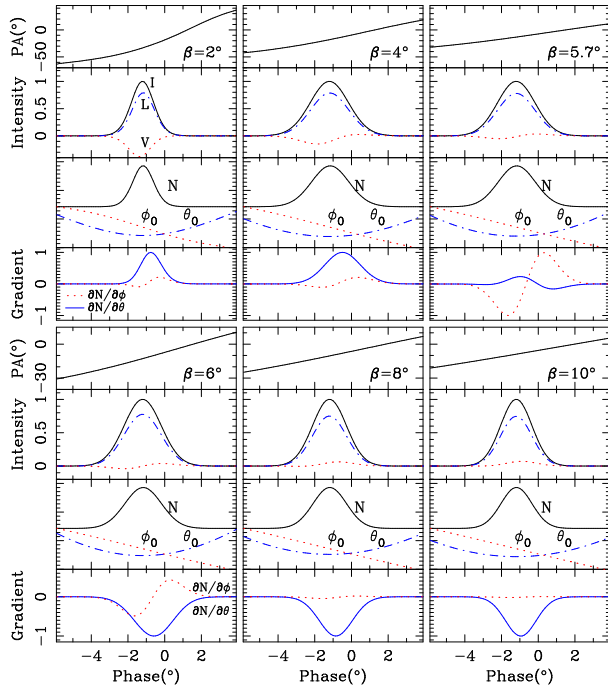
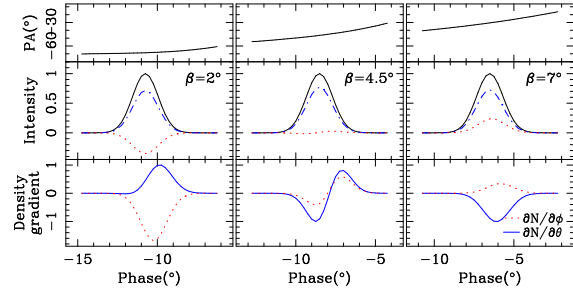


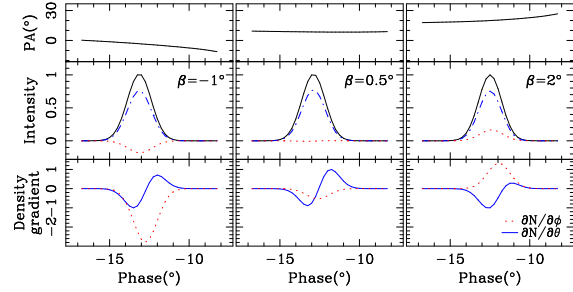
Figure 13. Same as Fig. 10 but for the density in a patch at $\phi_p = 0$ with $r = 50 R_*$. Profiles for six impact angles are shown. We plot $\partial N / \partial \phi / (\sin \theta)$ here instead of $\partial N / \partial \phi$, although marked as $\partial N / \partial \phi$ in the figure. The other parameters chosen here are $P = 1s$, $\nu = 400$ MHz, $\alpha = 30^\circ$, $\gamma = 400$, $s = 0.7$, $\sigma_{\theta_*} = 0.0006$ and $\sigma_\phi = 0.1$.

gradient along θ and ϕ . For a given patch, different cuts of a line of sight will cause different profiles. Here, we calculate the profiles for typical patch positions in the open field line region, with various impact angles. Figure 12 is the sketch map of the positions of the discussed patches.

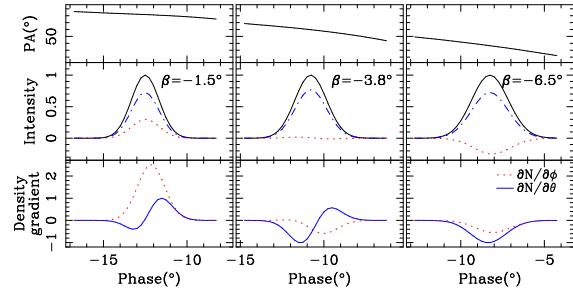
Firstly we consider a patch located in the meridional plane with $\phi_p = 0$. Sight lines cutting the patch with different β give different polarization profiles, as shown in Fig. 13.



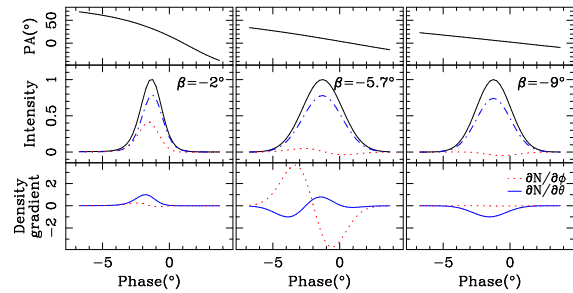
(a) $\phi_p = 45^\circ$



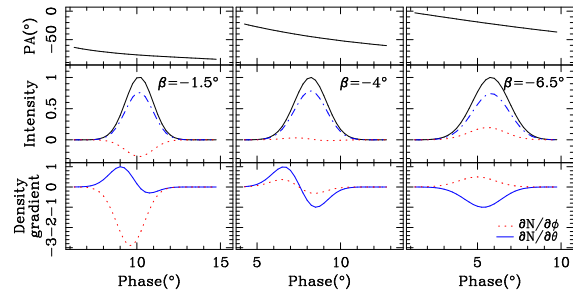
(b) $\phi_p = 90^\circ$



(c) $\phi_p = 135^\circ$



(d) $\phi_p = 180^\circ$



(e) $\phi_p = 225^\circ$

Figure 14. Same as Fig.13 but for other patches in Fig. 12.

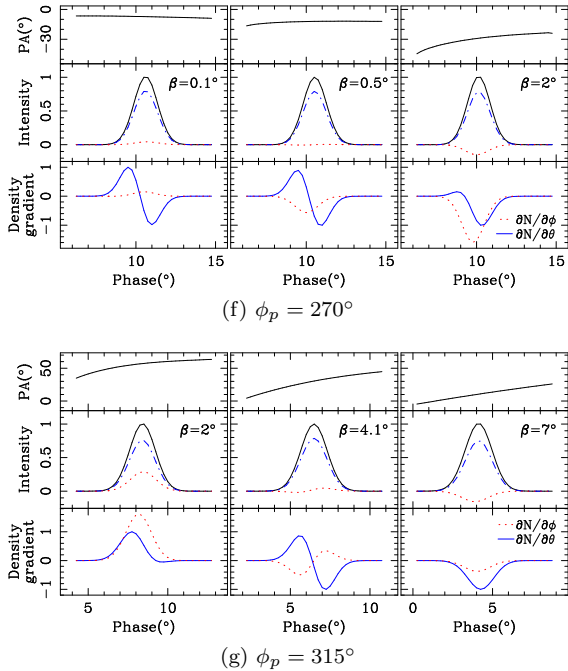


Figure 14. —continue

For $\beta = 2^\circ$, the dominating density gradient is $\partial N/\partial\theta$, which is large and has a single sign at all the phases, and $\partial N/\partial\phi$ is small. The circular polarization keeps to be of the right hand. When β increases to be 4° , there exits a little sign reversal of CP in the trailing side of the profile, mainly because $\partial N/\partial\phi$ is relatively strengthened. For the sight line cuts across the patch center of $\beta = 5.7^\circ$, $\partial N/\partial\theta$ reaches its minimum, $\partial N/\partial\phi$ dominates. The weak circular polarization shows a sign reversal. For large $\beta > 5.7^\circ$, negative $\partial N/\partial\theta$ dominates again gradually, which gives the reversal of weak CP and then the left hand CP.

Now, we consider the discrete patches (see Fig. 12) located at different positions around the magnetic axis with $\phi_p = 45^\circ, 90^\circ, 135^\circ, 180^\circ, 225^\circ, 270^\circ$ and 315° . The polarized profiles from cutting through the inner, central and outer parts of the patch are plotted for each patch in Fig.14. Similar to the patch of $\phi_p = 0^\circ$, the V profiles always have a single sign, or the sign reversal, or the opposite sign for the line of sight cutting the inner, central and outer parts of a patch. For the patches at $\phi_p = 90^\circ$ and 270° , we have $V \sim 0$ when the line of sight cuts across the central part of the patch. The V profiles for the patch at $\phi_p = 180^\circ$ has almost the same dependence on β as the patch of $\phi_p = 0^\circ$, except for the reversed circular polarization. For other patches away from the meridional plane, the V profiles always depend on the variation of $\partial N/\partial\phi$ and $\partial N/\partial\theta$ as listed in Table 1. But for patches with ϕ_p not close to 0° or 180° , the density gradient along ϕ dominates the sign of circular polarization, because the rotation-induced distortions are weak. For convenience, we mark the final sign of the V profile for different β in each patch of Fig. 12.

For a given patch, even when the impact angle β is fixed, the polarization profiles will be different for various emission heights. The polarized emission from two symmetrical patches with a fixed β but different height ($10R_*$, $20R_*$ and $40R_*$, respectively) are shown in Fig. 15. Naturally pro-

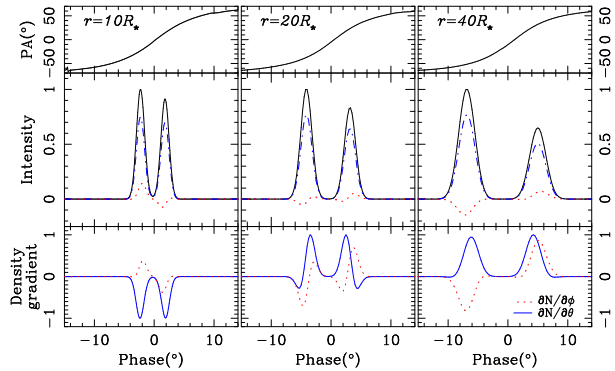


Figure 15. Same as Fig.13 but for two symmetrical patches ($\phi_p = \pm 30^\circ$) at heights of $10R_*$, $20R_*$ and $40R_*$. The impact angle is fixed to be $\beta = 3^\circ$. The other parameters used here are $P = 1s$, $\nu = 400$ MHz, $\alpha = 30^\circ$, $\gamma = 400$, $s = 0.7$, $\sigma_{\theta_*} = 0.001$ and $\sigma_{\phi} = 0.15$.

files gradually become wider with the increasing of height. They also gradually shift towards an earlier phase due to the aberration effect. The most important is the evolution of the circular polarization with emission heights. At a low height of $10R_*$, two components have different signs of CP, and each with one sign only. At a height of $20R_*$ (the middle panel), each component has the sign reversal of CP. At a height of $40R_*$, each component has one sign of CP again without reversal but the opposite hand compared to those at $10R_*$. This is mainly because at different heights, the sight lines with a fixed β cut through the inner, middle and outer parts of the patches, which should have different circular polarization due to the dominating of $\partial N/\partial\phi$.

4 EMISSION FROM OPEN FIELD LINE REGION

In general, a dipole field is assumed for pulsar magnetosphere. The tangential points of the field lines of $\theta \simeq 2/3\theta_{nm}$ can produce emission detectable for a given line of sight \mathbf{n} . Here θ_{nm} is the angle of the sight line from the magnetic axis \mathbf{m} , and $\theta_{nm} = \beta$ when the sight line goes to the meridional plane. Curvature radii are different for the tangential points at different heights, so that characteristic emission frequencies are different. This is the basic principle for the “radius to frequency mapping”. However, the emission from one height actually has a wide-spread spectrum, the characteristic frequency is only the frequency of the peak-intensity.

In fact, one receives the emission from the whole radiation region as long as the line is of $\theta \simeq 2/3\theta_{nm}$ in the open field line region (see Fig. 16). The retardation effect should be considered for the emission from different heights. The emission profile from the whole open field line region is given by

$$I(\varphi) = \int I_r(\varphi + r/r_{lc})dr,$$

$$Q(\varphi) = \int Q_r(\varphi + r/r_{lc})dr,$$

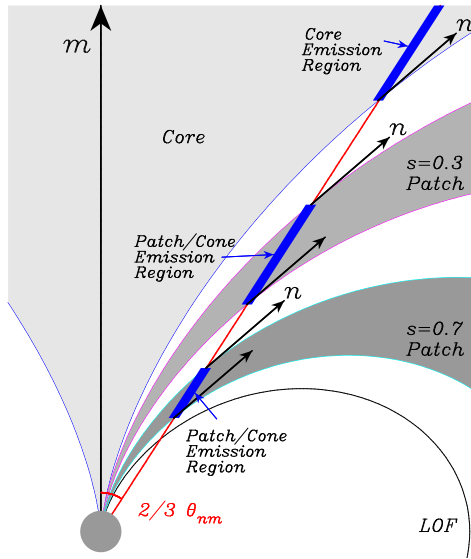


Figure 16. Emission regions for different density models. The thick line outlines all the tangential emission points of field lines of $\theta \simeq 2/3\theta_{nm}$ for a given line of sight, with θ_{nm} as the angle between wave vector \mathbf{n} and magnetic momentum \mathbf{m} . The grey areas represent the emission regions for the core and cone/patch regions.

$$\begin{aligned}
 U(\varphi) &= \int U_r(\varphi + r/r_{lc})dr, \\
 V(\varphi) &= \int V_r(\varphi + r/r_{lc})dr.
 \end{aligned} \quad (20)$$

Here I_r , Q_r , U_r and V_r are given by equation (16), and r/r_{lc} is the retarded phase for the emission from different heights.

The emission from a patch in the meridional plane with $s = 0.7$ is plotted in Fig. 17a, with the polarization generated at different phases and heights. The peak intensity I_p (given by equation 16) varies with the heights. The significant contribution to the integrated emission profiles in the bottom panel comes from the region of $8-20R_*$. For $r < 8R_*$ and $r > 20R_*$, the emission from this patch points away from the observer (see the sketch map of Fig. 16). The dominating contribution comes from the peak height around $r \simeq 12R_*$ for the maximum of plasma density (see the dashed line in the left panel of Fig. 17a). For the patch with a higher and wider emission region of $s = 0.3$ (Fig. 17b), the dominating emission comes from the height of about $130R_*$. There the aberration and retardation effects are rather strong, and the phase for the peak intensity and CP are shifted to an early phase.

We plot the emission profiles from the peak height in Fig. 18, which are very similar to the integrated total intensity and polarization profiles. The emission from the peak height always has a sign reversal of the circular polarization, because the density gradient along the magnetic azimuth ϕ has the sign reversal. The aberration and retardation effects are very weak for $r = 12R_*$ and the depolarization effect is also negligible.

We noticed that the polarization profiles from a patch are almost the same for different frequencies. If the patch is wide and the density gradient is small, e.g. the almost uniform distribution, the net circular polarization from a patch

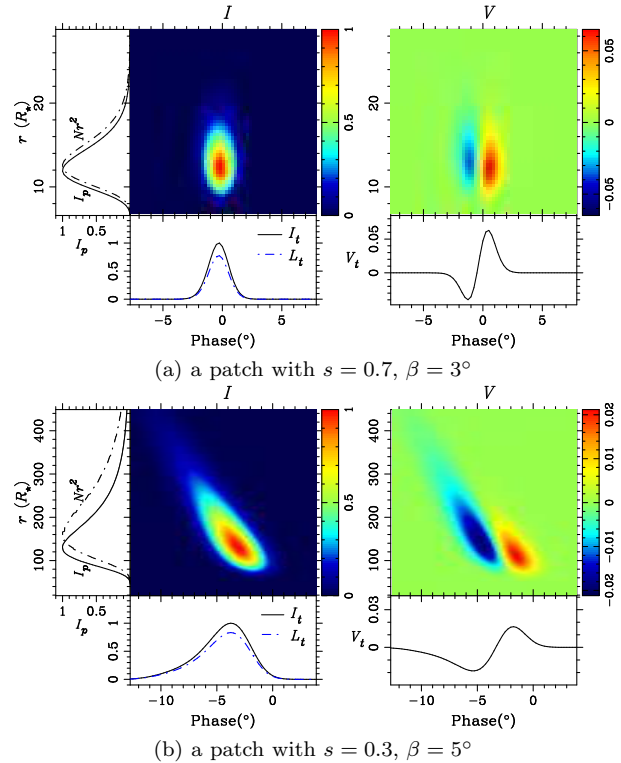


Figure 17. Total intensity and circular polarized emission of the curvature emission from two patches, plotted for various phases and heights. The linear polarization is very similar to the total intensity I except for a slightly smaller magnitude. The integrated emission profiles are plotted under each map. The variations of the peak intensity I_p (solid line) and Nr^2 (dash-dotted line) are also plotted against heights in the left. The pulsar parameters used here are the same as those in Fig. 13.

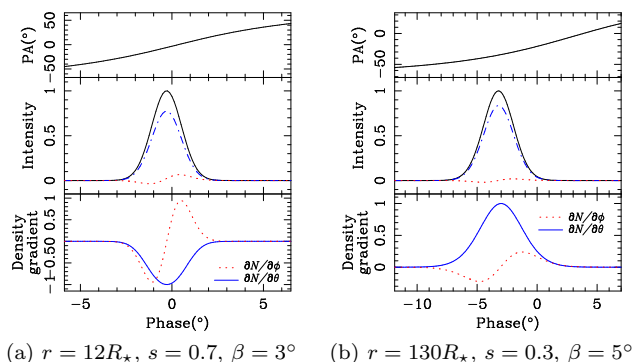


Figure 18. The emission profiles from the peak heights of the two patches in Fig. 17.

should be very small. Note however that the peak height is different for different frequencies, and the integrated circular polarization may change for different frequencies.

For the core density model, the emission region of $\theta = 2/3\theta_{nm}$ does not have an upper limit (see Fig. 16). The intensities from various emission heights, up to thousands of R_* , are still significant compared with that from the peak height of $r \sim 250R_*$ (see Fig. 19a). It is related to the integrand term Nr^2 in equation (16), which determines the final value of I_p . The density variation can be written as

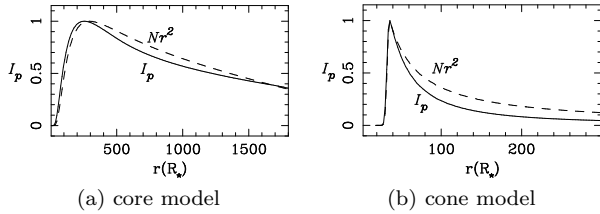


Figure 19. The peak intensity varies with the heights (solid lines) for core density model (panel a), and for cone model (panel b). The density variations, Nr^2 , are also plotted with the dashed lines. The parameters are the same as those in Fig. 10 for core and Fig. 11 for cone.

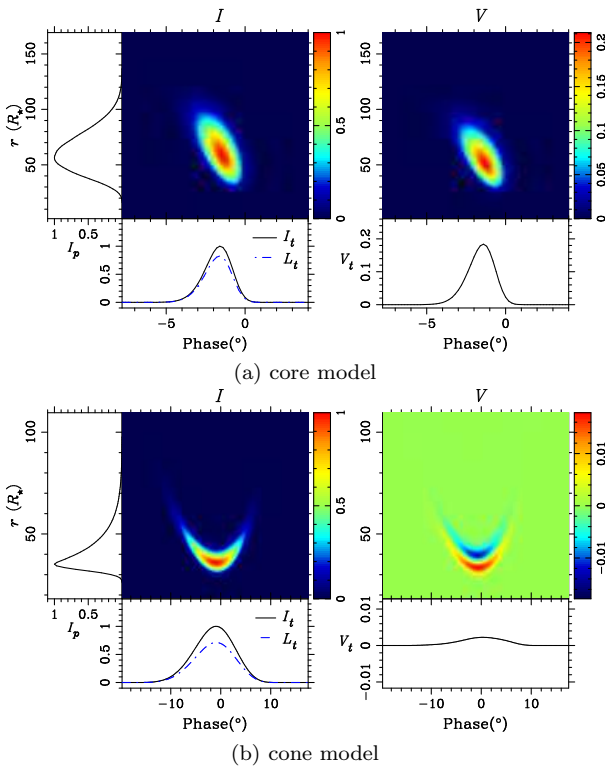


Figure 20. Same as Fig. 17, except for the curvature emission from core (panel a) and cone (panel b). Lorentz factor damping along the particle trajectory is assumed as equation 22, with an initial Lorentz factor at the star surface of $\gamma_0 = 1000$ and the damping factor $\kappa_\gamma = 0.01$. The other parameters used for calculation here are the same as those in Fig. 19.

$$Nr^2 = n(r)f(\theta)g(\phi)r^2 \propto r^{-1} \exp\left(-\frac{\theta^2}{2\sigma_{\theta_*}^2} \frac{R_*}{r}\right), \quad (21)$$

and plotted by the dashed line in Fig. 19a. The total emission profile is very wide in phase because of the retarded emission from large heights, and the polarization will also be vanished.

In a practical case, the damping of the Lorentz factor of a particle along r is natural. For example, an exponential decay of the Lorentz factor was introduced by Qiao et al. (2001) to analyze the inverse Compton scattering process in the magnetosphere. Here we take the slow variation of the Lorentz factor with height as

$$\gamma = \gamma_0 \exp\left(-\kappa_\gamma \frac{r - R_*}{R_*}\right), \quad (22)$$

where γ_0 is the energy for the secondary particles near the neutron star polar cap, and κ_γ is the damping factor, and we calculate the total emission profiles as shown in Fig. 20a. The emission region is constrained to be between $20R_*$ and $120R_*$. The total polarized profiles resemble to those from a height of $50R_*$ (Fig.10). The circular polarization contributed from each height has the same sign, so the final total circular polarization has only one single sign. The total intensity and polarization profiles are asymmetry due to the retardation effect.

For the cone density model, the density Nr^2 and the peak intensity vary with height as shown in Fig. 19b. The emission can be produced even at a very large height. The dominating emission comes from about $30R_*$ to $300R_*$. The profiles become very wide (see Fig.20b) because of the strong retardation effect. With the damping of the Lorentz factor of particles as the core model, the total emission profiles and $I_p(r)$ are shown in Fig. 20b. The cone density only produces one profile component, instead of two. Because the emission from low heights are very strong, and two components from a higher regions are weak and only add the outer wings in both sides of the profile from the lower height. The total circular polarization is very weak also, because of the depolarization of the emission from different heights.

5 DISCUSSIONS AND CONCLUSIONS

In this paper, we depict the detailed scenery for curvature radiation in rotating pulsar magnetosphere for the first time. The rotation affects the velocity and acceleration of particles and hence the emission property. Circular path approximation for the particle trajectory is used at the emission point to calculate the radiating electric field (see equation 13). The emission from particles at the tangential points of field lines and the nearby field lines in the $1/\gamma$ emission cone is considered for a given phase and height. The polarization profiles from a given height and the whole open field line region are calculated for three possible density distributions in the form of core, cone and patches. We find the following conclusions:

(i) Rotation not only shifts the PA curves along the rotation phase, $\Delta\varphi_0$, but also causes an offset of the curve, ϕ_{PA0} , both of which are the first-order functions of the emission height. Its influences on α and β determination follows the second order functions (Fig. 8).

(ii) Rotation distorts the patterns for the $1/\gamma$ cone more seriously if it originates from larger height and/or smaller impact angle (Fig. 9). The density gradients across the patterns will result in the net circular polarization.

(iii) For the patch density model, the V profiles from the same height can have a single sign or the sign reversal or the opposite sign, depending on where the sight line is cutting (Fig. 13,14). The polarization profiles resulting from a fixed impact angle also vary with emission heights (Fig. 15).

(iv) The central peaked core will have the circular polarization of only one hand, which is usually significant and always has a single sign (Fig. 20a). The cone emission at a large height is separated into two components with the opposite sign reversals for circular polarization. But at a lower height there is only one component with a single sign of V . The total circular polarization is very weak because

of the depolarization of the emission from different heights (Fig. 20b).

Our calculations for the curvature radiation from particles distributed in the form of core, cone and patches can be compared with the observed pulsar polarization profiles. The sign reversal of circular polarization are always observed in the central component of the mean profile (Lyne & Manchester 1988; Rankin 1983; Gil & Snakowski 1990). Han et al. (1998) pointed that there also exists sign reversal of circular polarization for the cone components for some pulsars. Such observational facts can be explained if the emission comes from central or non-central patches. The CP with a single sign may come from the core emission.

Here we did not consider the possible propagation effects, i.e., the wave mode coupling effect (Wang et al. 2010) in the magnetosphere. Our calculations can explain some pulsar polarized emission, but it can not match various observation facts. It should be noted that we consider just the curvature emission from particles with a single γ and assume the simple distributions of particle density. The actual energy and density distributions of particles in the magnetosphere are not clear at present. There exist other emission mechanisms, like ICS (Xu et al. 2000), plasma process (Beskin et al. 1988). Moreover, we treated the coherency in a simple way by assuming the coherent bunch to be a huge point charge. However, the actual coherent manner, bunch size and shape affect the radiation pattern (Benford & Buschauer 1977). We used the vacuum dipole magnetic field as the basic model for our calculation, but there exists the possible distortion of the dipole magnetic field due to rotation, which has not been taken into account (Dyks & Harding 2004). The magnetic field structure, such as the globally twisted, self-similar, force-free magnetosphere (Thompson et al. 2002), can also lead to the modification of the radiation pattern. All these will make the actual emission pattern much more complicated than the simple calculations presented in this paper.

ACKNOWLEDGMENTS

We thank R. T. Gangadhara and Dinesh Kumar for useful discussions and suggestions. This work has been supported by the National Natural Science Foundation of China (11003023 and 10833003).

REFERENCES

- Backer D. C., 1976, ApJ, 209, 895
 Benford G., Buschauer R., 1977, MNRAS, 179, 189
 Beskin V. S., Gurevich A. V., Istomin I. N., 1988, Ap&SS, 146, 205
 Blaskiewicz M., Cordes J. M., Wasserman I., 1991, ApJ, 370, 643
 Buschauer R., Benford G., 1976, MNRAS, 177, 109
 Dyks J., Harding A. K., 2004, ApJ, 614, 869
 Dyks J., Wright G. A. E., Demorest P., 2010, MNRAS, 405, 509
 Gangadhara R. T., 2005, ApJ, 628, 923
 Gangadhara R. T., 2010, ApJ, 710, 29
 Gil J. A., Snakowski J. K., 1990, A&A, 234, 237
 Han J. L., Manchester R. N., Xu R. X., Qiao G. J., 1998, MNRAS, 300, 373
 Hibschan J. A., Arons J., 2001, ApJ, 546, 382
 Jackson J. D., 1975, Classical electrodynamics
 Komesaroff M. M., Morris D., Cooke D. J., 1970, Aplet, 5, 37
 Kumar D., Gangadhara R. T., 2012, ApJ, 746, 157
 Lyne A. G., Manchester R. N., 1988, MNRAS, 234, 477
 Oehlke I. P., Usov V. V., 1980, Ap&SS, 69, 439
 Qiao G. J., Liu J. F., Zhang B., Han J. L., 2001, A&A, 377, 964
 Rankin J. M., 1983, ApJ, 274, 333
 Rankin J. M., 1993, ApJ, 405, 285
 Rankin J. M., Ramachandran R., 2003, ApJ, 590, 411
 Ruderman M. A., Sutherland P. G., 1975, ApJ, 196, 51
 Thomas R. M. C., Gangadhara R. T., 2007, A&A, 467, 911
 Thompson C., Lyutikov M., Kulkarni S. R., 2002, ApJ, 574, 332
 Wang C., Lai D., Han J., 2010, MNRAS, 403, 569
 Xu R. X., Liu J. F., Han J. L., Qiao G. J., 2000, ApJ, 535, 354